CHAPTER 5

Microstructural, Ferroelectric, Piezoelectric and Dielectric Properties of $(1-x)Ba(Cu_{1/3}Nb_{2/3})O_3$-$(x)PbTiO_3$ Ceramics

CHAPTER 5.

Microstructural, Ferroelectric, Piezoelectric and Dielectric Properties of (1-x)$Ba(Cu_{1/3}Nb_{2/3})O_3$-(x)$PbTiO_3$ Ceramics

5.1 Introduction

Exploration of the dielectric and piezoelectric properties of MPB compositions and their correlation with structure is popularly studied topic in Pb-based piezoelectric ceramics such as PZT, PMN-xPT, etc. [12,40,41] These ceramics are the market leaders in the dielectric materials-based industries due to their excellent piezoelectric, dielectric, and ferroelectric properties [37]. As discussed in chapter 1, these ceramics are being discouraged in use due to the serious concern of the toxicity of Pb. In recent years, new piezoelectric ceramics with reduced Pb concentration, without compromising their piezoelectric and dielectric properties, are being looked at, with great interest. Some other new PT-based alike solid solutions such as (1-x)$Ba(B'_{1/3}Nb_{2/3})O_3$-x$PbTiO_3$ (B' = Mg, Yb, Zn and Lu) were investigated and most of these systems possess an MPB with a rhombohedral-tetragonal phases between $0.71 \leq x \leq 0.74$, $0.65 \leq x \leq 0.70$, $0.58 \leq x \leq 0.61$, $0.64 \leq x \leq 0.68$ and $0.61 \leq x \leq 0.65$ composition ranges for B' = Mg, Yb, Zn and Lu, respectively [63–68]. These solid solutions possess d_{33} in the range of 100~150pC/N and P_r in the range of 10~18μC/$cm^{2,}$ while T_c was observed around 55~250°C [63–68].

Prior to our work, Priya et al. (2002) have briefly investigated (1-x)BCN-(x)PT solid solution with x = 0.90 and x = 0.95 compositions only [47]. Thus, there was no report for this system, on the location of the morphotropic phase boundary and the

characterization of various physical properties of MPB compositions. In view of this, we have investigated microstructural, dielectric, ferroelectric, and piezoelectric properties of the (1-x)BCN-(x)PT solid solution in the wide compositional range especially close to the MPB region. In this chapter, we present the results of the microstructure, dielectric, ferroelectric and piezoelectric characterizations of this solid solution over the full composition range and their correlations are established with crystal structure. The temperature dependent dielectric investigation of the selected representative compositions has been done to comprehend the study. The compositional homogeneity and stoichiometric valences of constituent ions in selected compositions have also been verified with EDS and XPS for correlating it with the observed physical properties.

5.2 Microstructural Studies of (1-x)BCN-(x)PT Ceramics

The SEM microstructural characterizations have been performed for different compositions spread throughout the solid solution. SEM images of some of the representative sintered ceramics pellets with composition (a) x = 0, (b) 0.20, (c) 0.40, (d) 0.55, (e) 0.60, (f) 0.65, (g) 0.70, (h) 0.80 and (i) 0.90 are shown in Fig 5.1. All the ceramics were sintered at 1050°C for 2 hours, except for BCN, which was sintered at 1150°C for 4 hours. Fig 5.1(a) corresponds to pure BCN, in which the average grain size is around 1µm. Due to the liquid phase sintering at the surface, the grain size in x = 0.20, 0.40 and 0.55 compositions is found to be 1.9 µm, 2.2 µm and 1.3 µm. Additionally, the high calcination temperatures for the x = 0.20 and 0.40 compositions are also reflected in their larger grain sizes. The grain size further decreases in the x = 0.62 and 0.65 compositions with an average grain size of 1µm and 0.5µm. Similarly, in the composition region of $0.70 \leq x \leq 0.85$, the calcination temperature is increased to

975°C; therefore, a comparative increment in grain size is observed in the x = 0.70 composition with an average grain size of 0.83μm. The grain sizes of the x = 0.80 and 0.90 compositions are obtained as 0.35μm and 0.25μm, respectively.

In ceramics, microstructure, especially the grain size, shares its dependency with powder milling time and high-temperature treatment [77,123–125]. To achieve a pure phase in the BCN sample, a longer time for ball milling (12 hours) was needed, while long calcination (10 hours at 900°C) was required to form the perovskite phase. Being a fragile composition due to high tetragonal lattice strain (c/a = 1.033) BCN was sintered at high-temperatures (1150°C) to achieve maximum densification with the lowest possible cracking and melting compared to other compositions of the solid solution.

The average grain size shows a decreasing trend with increasing PT content in the second half composition range ($0.50 < x < 1$), as can be seen from Fig 5.2. In high Cu content compositions of the solid solution, i.e., in the first half composition range ($0 < x \leq 0.55$) partial melting at the surface is observed [126] due to which the estimation of accurate grain structure is hampered, and is highly depended on the measurement depth of the sample. The experimentally measured densities of the $0.20 \leq x \leq 0.75$ compositions are 99%, whereas the same reduces from 97% to 93% for higher high PT compositions, which can also be visualised from the SEM micrographs.

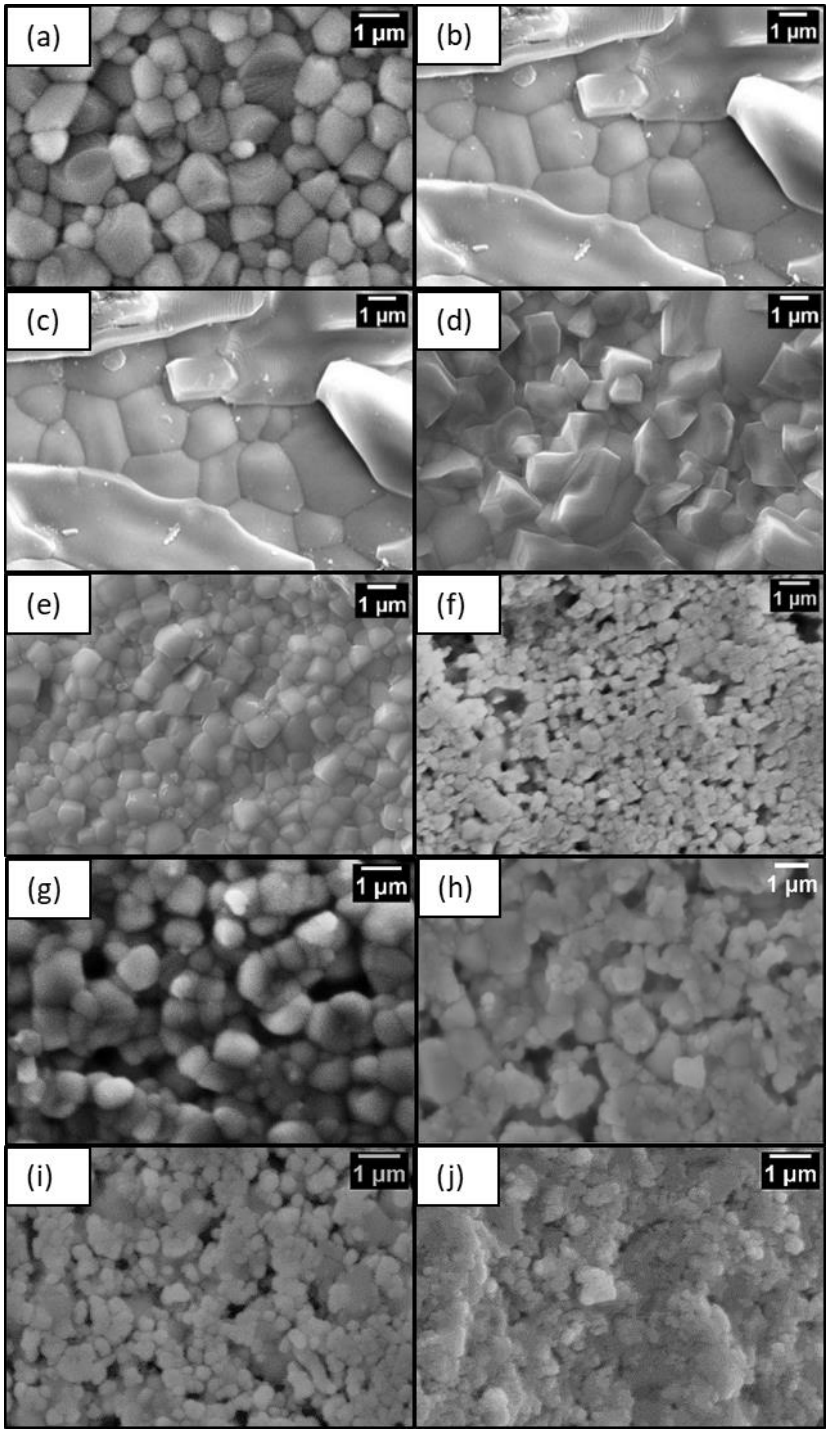

Fig 5.1 SEM images of sintered (1-x)BCN-(x)PT ceramics with composition x = (a) 0, (b) 0.20, (c) 0.40, (d) 0.55, (e) 0.62, (f) 0.65, (g) 0.70, (h) 0.75 (i) 0.80 and (j) 0.90

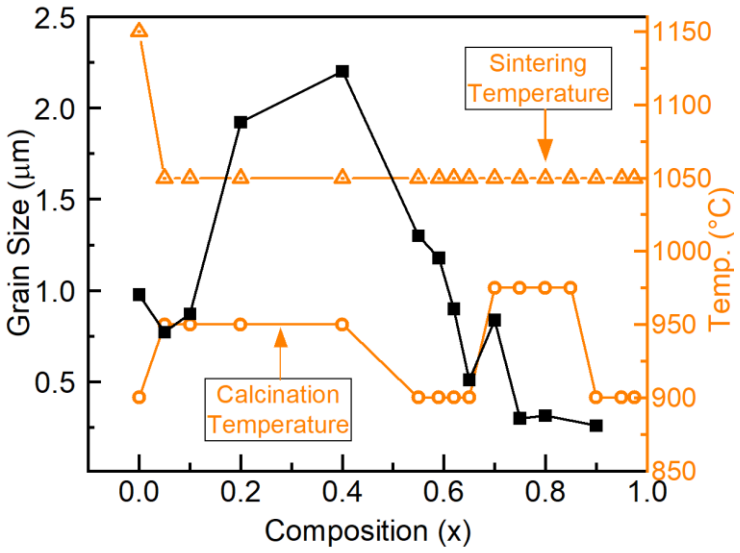

Fig 5.2 Variation of the grain size for different heat treatment of calcination and sintering temperature in (1-x)BCN-(x)PT ceramics

5.3 Compositional Analysis of (1-x)BCN-(x)PT from EDS and XPS

Chemical homogeneity and quality of the samples are very crucial factors in deciding the physical properties of ceramic solid solutions. To better correlate the dielectric, ferroelectric and piezoelectric properties of (1-x)BCN-(x)PT ceramics with location of MPB and phase coexistence, the compositional analysis of the sample has been performed. For the compositional investigation, the x = 0.80 composition has been chosen because the phase fraction of both the coexisting tetragonal and monoclinic phases in this composition are nearly 50/50. Fig 5.3 shows the EDS measurement results on a fractured surface of a pellet of x = 0.80 composition. A grain structure of shallow contrast is visible in Fig 5.3(a), possibly due to the fracturing between the grains. Fig 5.3(b-g) shows the elemental mapping of the Nb, Ti, Cu, O, Pb and Ba ions, respectively. These pictures show a homogeneous distribution of ions and the absence of any segregation of phases at the microscale. This indicates that the observed

crystallographic phase separation discussed in chapter 3 and 4 for the x = 0.80 sample, is not due to inhomogeneity in the composition or a particulate composite kind of micro-scalar phase segregation. The compositional distribution of ions in the samples has been verified by EDS as well as by XPS analysis. Fig 5.3(h) shows the histogram of the atomic weight % of different elements in the x = 0.80 composition using EDS spectra. It can be seen from this figure that the constituent elements (Ba, Cu, Nb and Ti) of the solid solution composition present in the sample are close to the nominal composition ratio within the limit of experimental error. The high-temperature losses in Pb content are also observed. The error in assessing the oxygen concentration is high, which can be the reason behind its comparatively high content.

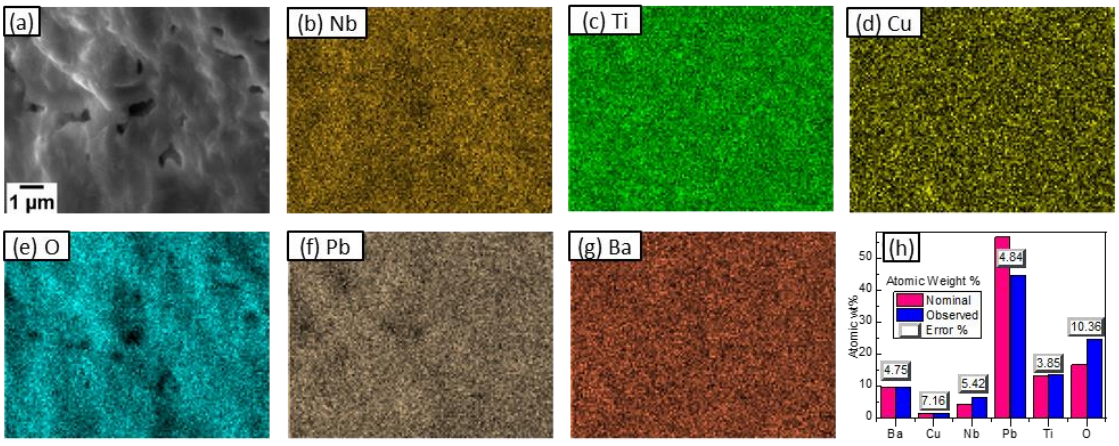

Fig 5.3 EDS elemental mapping of the x = 0.80 composition. (a) SEM image of a fractured surface, Elemental mapping of (b) Nb, (c) Ti, (d) Cu, (e) O, (f) Pb, (g) Ba over the SEM image region; (h) histogram showing the experimental atomic weight % observed from the EDS and calculated from stoichiometric nominal composition.

In the XPS analysis, the surface of the sintered pellet is prepared by polishing in such a way to exfoliate the heat treatment exposed surface, followed by cleaning and annealing of the surface. Although the surface studied in the XPS still belongs to the

portion only ~0.1mm below the surface, it can be roughly approximated to get an idea about the probable valence state of the constituting ions in the bulk samples. The XPS analysis has been done for two compositions belonging to the two types (x = 0.62 and x = 0.85) of phase coexistence regions. As these are far apart from each other in terms of composition content, they can be used to roughly represent all solid solution compositions. The XPS results of the composition x = 0.62 [127] are covered in the next chapter, while the same for the composition 0.85 are as follows:

The oxygen vacancies present in the sample during heat treatment attract the surface hydroxyl group, which corresponds to the higher binding energy shoulder to the O-1s peak in XPS around 529eV as can be seen in Fig 5.4(a)] [128]. In Fig 5.4(b-f), the XPS data of all the cations in the solid solution composition x = 0.85 is shown to verify the oxidation states of all the constituent ions. In the standard XPS pattern of CuO, the characteristic peak for the Cu-2p orbital splits by 19.75eV due to spin-orbit coupling, leaving the binding energy (B.E.) of Cu-$2p_{3/2}$, around 933.6eV and Cu-$2p_{1/2}$ at 953.4eV, containing strong shake-up satellites around 942.4eV, 944.6eV and 963.3eV [129]. These satellites are weak in Cu_2O. In Fig 5.4(b), the Cu-2p spectra is shown, which confirms the presence of Cu-ion in the '+2' state with the observation of peaks as mentioned above. However, small concentrations of copper ions in '+1' states cannot be efficiently separated in these XPS studies due to the overlapping positions of satellites. The Nb-3d spectra possess B.E. peaks of $3d_{5/2}$ and $3d_{3/2}$ around 209.3eV and 206.6eV in the perovskite structure [130]. Fig 5.4(c) shows the Nb $3d_{5/2}$ peak is observed at 206.2eV with a nominal gap of 2.7eV between the $3d_{5/2}$ and $3d_{3/2,}$ confirming the single '+5' state of Nb. The Ti-2p XPS spectra of titanium oxide have two components, $2p_{3/2}$ and $2p_{1/2,}$ in B.E. peaks, and they are separated by approximately 5.7eV for ‘+4’ state of

Ti [131]. The B.E. of $2p_{3/2}$ for Ti^{+4} is 458.7eV (±1.3eV) [132]. The Ti-$2p_{3/2}$ is observed around 257.5eV with a separation of 5.7eV between $2p_{3/2}$ and $2p_{1/2}$, in Fig 5.4(d). This confirms the '+4' state of Ti (see). Similarly, the Ba-3d peak in pure BaO appears at 778.5eV with a B.E. gap of 15.33eV between the $3d_{5/2}$ and $3d_{3/2}$ peak splitting [133]. Fig 5.4(e) shows similar values, with the appearance $3d_{5/2}$ B.E. peak at 779eV. Pure PbO shows a 4f peak splitting of 4.8eV with $4f_{7/2}$ at 136.8eV [134]. A doublet splitting of 4.87eV is observed for $4f_{7/2}$ at 137.6eV for the composition x = 0.85 in the perovskite phase, as shown in Fig 5.4(f). Therefore, all the elements are present in their nominal compositional content and valence state. The XPS analysis of the 0.62 composition also shows the nominal valence states of the constituent ions (Section 6.5).

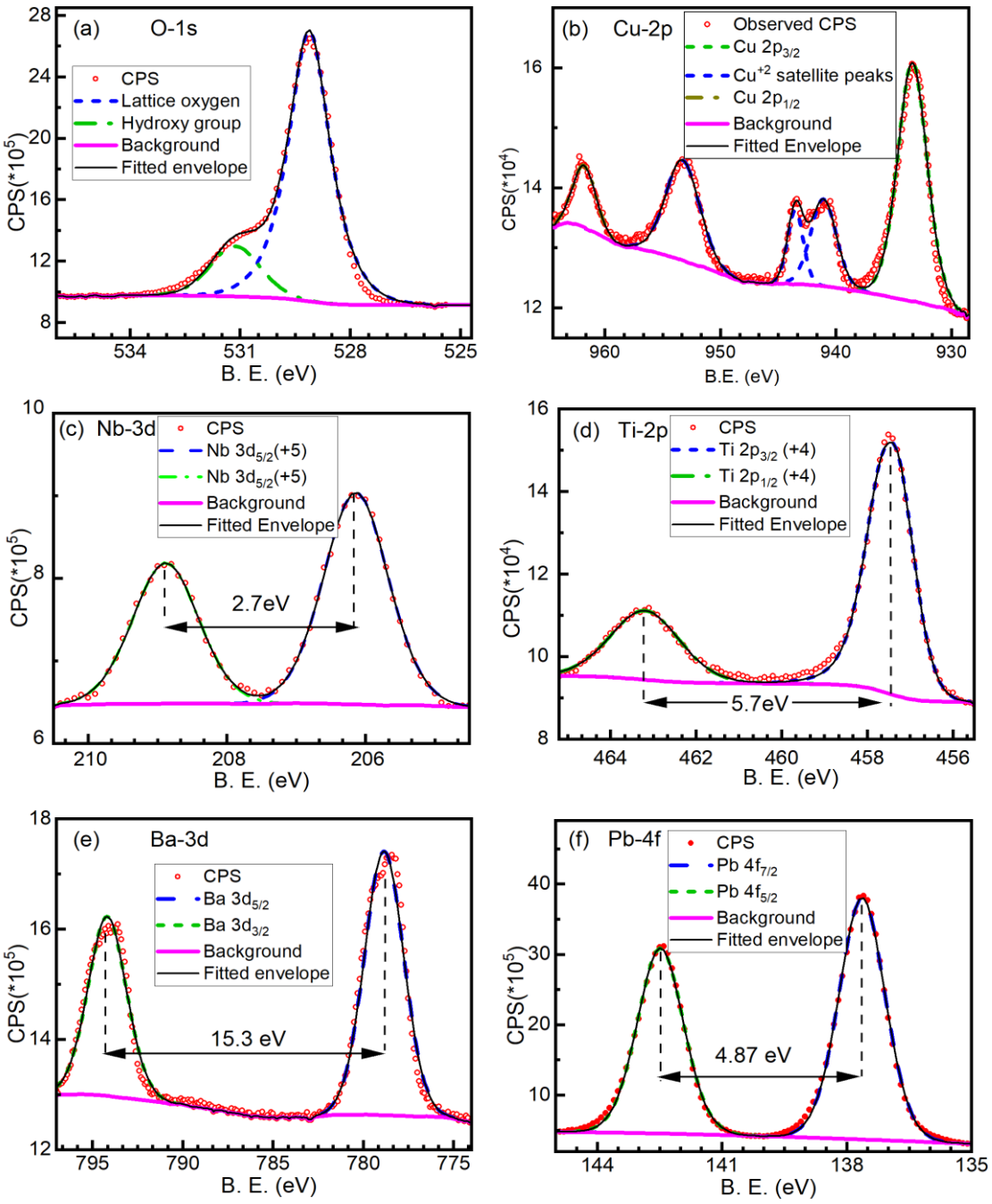

Fig 5.4 XPS spectra of (a) O-1s, (b) Cu-2p, (c) Nb-3d, (d) Ti-2p, (e) Ba-3d and (f) Pb-4f orbitals of (0.15)BCN-(0.85)PT composition

5.4 Dielectric Studies on (1-x)BCN-(x)PT Ceramics

Temperature-dependent dielectric measurements were performed on platinum electroded pellets from RT to 500°C at a heating rate of 2°/min. Fig 5.5(a) and Fig 5.5(b) show the relative dielectric permittivity (ε_r) in the composition range $0.20 \leq x \leq 0.65$ and $0.70 \leq x \leq 0.975$, respectively. Fig 5.5(c) and Fig 5.5(d) show the dielectric loss ($\tan\delta$) in the composition range $0.20 \leq x \leq 0.65$ and $0.70 \leq x \leq 0.975$, respectively.

Crystal structural phase transitions and defect (mobile and dipolar) relaxations are often accompanied by the observation of peak/anomaly in the temperature-dependence of dielectric permittivity responses [135]. The nature of these peaks in terms of sharpness, diffusiveness and frequency dispersion characteristics defines their characteristics as belonging to the relaxor category, first order/second order phase transition, etc. Furthermore, some dielectrics show permittivity peaks in the temperature dependence at lower frequencies but not at higher frequency responses for the same temperature region. Such a response generally arises due to Maxwell-Wagner relaxations, in which mobile charge carriers play vital roles [136]. Such contributions are minimised at higher frequencies of 10 kHz and above. Therefore, all these responses in Fig 5.5(a-d) are given for 10 kHz frequency. The relative dielectric permittivity responses of the composition range $0.55 \leq x \leq 0.975$ have already been discussed briefly for the co-relations of crystal structure with the characteristic dielectric phase transition peaks in Section 4.2. Here, these are results are reproduced for their detailed comprehensive studies.

The compositions x = 0.20, 0.40 and 0.55 are the ones that possess cubic crystal structure at RT. Therefore, only temperature-dependent relaxation peaks are observed

for these compositions in relative permittivity as well as in dielectric loss responses. In Fig 5.5(a), the relaxation peak and their high responses at 10 kHz suggest a high concentration of defect relaxations [137]. As discussed in chapter 3 and 4, the (1-x)BCN-(x)PT solid solution possesses two kinds of crystallographic phase coexistence. In the composition regions $0 \leq x \leq 0.62$ and $0.95 \leq x \leq 0.975$, the phase fraction of dominant thermodynamic phase is so high that it can be considered a single system to understand the dielectric behaviour. These non-cubic compositions in this region exhibit only one dielectric permittivity peak corresponding to the ferroelectric to paraelectric phase transition. Two non-centrosymmetric crystallographic phases present in the compositions with phase separation show two dielectric transitions corresponding to each phase in the temperature-dependent relative dielectric permittivity responses. These peaks can be observed in Fig 5.5(b) for the compositions lying in the region $0.70 \leq x \leq 0.90$. Both the peak temperatures in Fig 5.5(b) have been successfully correlated with the phase transition temperatures in high-temperature XRD studies as discussed in the Section 4.2. The high responses in permittivity of the 0.65 and 0.75 compositions are due to the dominance of defect relaxation contributions. The solid solution compositions do not show the relaxor ferroelectric type nature of transitions as the temperature-dependent shift of peaks in frequency dispersion is absent. The RT dielectric constant gradually decreases with increasing PT content in the solid solution system.

In the compositions 0.60, 0.62 and 0.65, smaller peaks in the temperature region 80°C~150°C in Fig 5.5(c) correspond to the phase transition, whereas the more prominent peaks in them are mainly due to defect relaxations. These prominent relaxation peaks appear at 250°C, 200°C, 120°C and below RT for the 0.65, 0.55, 0.40

and 0.20 compositions, i.e., they shift towards lower temperatures with increasing BCN content in the solid solution. This indicates their origin as one kind. These transitions are suppressed for the 0.60 and 0.62 compositions, indicating comparatively lower losses. In the x = 0.65 composition, the loss peak corresponding to the Curie transition is masked by relaxations. The dielectric loss at RT also shows an increment with increasing BCN content for the $0.20 \leq x \leq 0.55$ composition region of the solid solution, while their low values are observed (below the 0.05 composition) for the composition range $0.70 \leq x \leq 0.95$. Along with the comparatively lower losses, the Curie transition peaks are also visible for some of these compositions in Fig 5.5(d). The Curie transition temperatures and dielectric constant at RT for all the compositions are listed in Table 5.1. The frequency-dependence of dielectric permittivity at RT for various compositions is depicted in Fig 5.5(e). It can be seen that the frequency dispersion decreases with increasing PT content. Increased PT concentration in the solid solution is expected to enhance the normal ferroelectric behaviour in the compositions.

Table 5.1 Comparison of dielectric, ferroelectric and piezoelectric response for different compositions of (1-x)BCN-(x)PT ceramics

Composition (x)	ε_r (RT)	T_{C1} (°C)	T_{C2} (°C)	d_{33} (at RT) (pC/N)	P_r (μC/cm^2)	P_s (μC/cm^2)
0.60	1734	70-85	-	4	1	1.6
0.62	825	127	-	2	1.7	1.8
0.65	1065	155	-	3	-	-
0.70	570	195	440-450	44	7.6	44.5
0.75	550	185	435	42	5.8	40.2
0.80	400	242	455	17	6.7	35.6
0.85	380	275	442	11	4.4	41.7
0.90	311	320-340	450	38	3.7	49
0.95	230	-		18	0.7	40.2

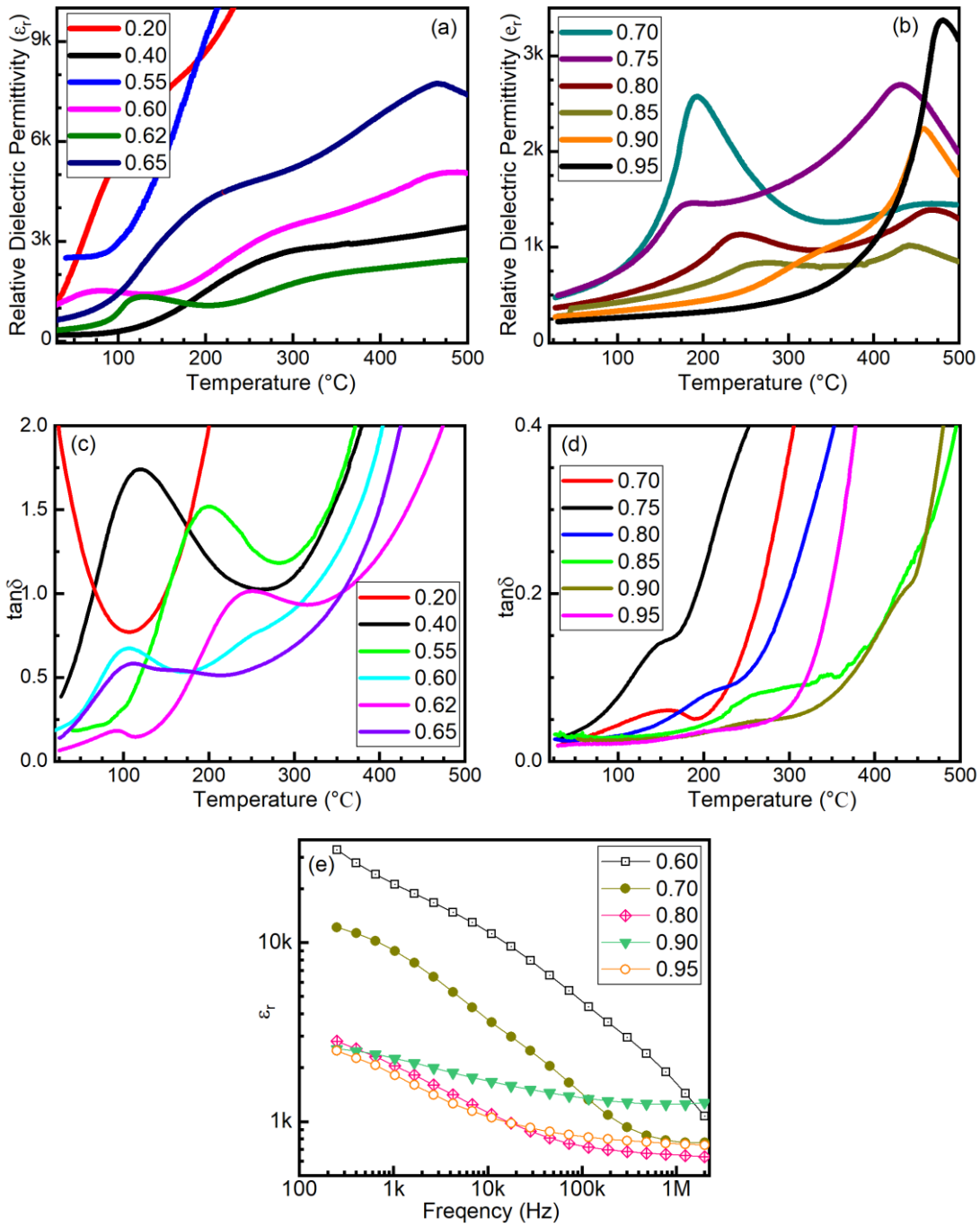

Fig 5.5 Temperature-dependent variation of relative dielectric permittivity for composition range (a) $0.20 \leq x \leq 0.65$ and (b) $0.70 \leq x \leq 0.95$, and dielectric loss in composition range (c) $0.20 \leq x \leq 0.65$ and (d) $0.70 \leq x \leq 0.95$ measured at 10 kHz; (e) RT frequency-dependence of relative permittivity; for various compositions of (1-x)BCN-(x)PT ceramics.

5.5 Ferroelectric Studies on (1-x)BCN-(x)PT Ceramics

The P-E hysteresis loops measured on the platinum electroded pellets of (1-x)BCN-(x)PT ceramics, for the composition range $0.55 \leq x \leq 0.975$, are shown in Fig 5.6(a). The compositions in the range $0.20 \leq x \leq 0.55$ possess a cubic crystal structure. The partial melting of the samples (as can be seen in Fig 5.1(b, c and d)), and the tendency of fluctuation in the oxidation states of copper ions lead to high losses in these compositions [47,138]. Therefore, pellets of these compositions could not be poled. Since the compositions $0.20 \leq x \leq 0.55$ are cubic paraelectric, an absence of ferroelectricity is evidenced by the unsaturated lossy loops of these compositions (see the inset of Fig 5.6(a)). In Fig 5.6(a), clear ferroelectric nature of P-E loops has been observed for the composition range $0.70 \leq x \leq 0.975$. An asymmetry in the P-E loops is also observed for almost all the compositions in this range. To find the various contributions in the measured polarization and confirm the ferroelectric domain switching, an instantaneous current loop measurement has been done and the results are shown in Fig 5.6(b) for the $x = 0.70$ and 0.90 compositions. A peak in the current corresponding to the coercive field indicates the switching of the ferroelectric domains, confirming the ferroelectric behaviour in these compositions. A linearly increasing and a constant current response are regarded as the contributions of leakage current and dielectric permittivity, respectively [138]. The current loops are also asymmetric, indicating the effect of high concentration of defects in the solid solution. The Pb loss and the Cu ion valency fluctuation from '+2' to '+1' are the potential defect species in the solid solution that may be caused by high-temperature sintering [47]. Since the P-E loops are measured after poling, high DC fields of poling provide sufficient energy for defects to move and deposit at grain and domain boundaries while simultaneously

aligning them to a field direction [139]. As a result, the domains are pinned and cannot switch to the opposite direction when applying a 50 Hz bipolar triangular electric field. Thus, all the P-E and I-E loops are asymmetric for the investigated ferroelectric compositions of (1-x)BCN-(x)PT. The composition-dependent remnant polarization (P_r) and coercive field (E_c) for the (1-x)BCN-(x)PT are listed in Table 5.1 and plotted in Fig 5.6(c). To correlate with the results of crystal structure analysis discussed in chapter 3 and 4, the monoclinic and tetragonal phase coexistence region is marked as 'M+T' and the phase boundaries are marked by vertical dashed lines in Fig 5.6(c).

For the x = 0.70 composition, the highest value of P_r has been observed. The room-temperature crystal structure of this composition has coexisting monoclinic and tetragonal phases, and it lies close to the MPB. The composition 0.70 exhibits the best ferroelectric nature amongst others, as it possesses a number of merits over its nearby compositions, such as large grain size, high densification and proximity to the MPB. The lower PT concentration compositions (x < 0.70) contain high losses, whereas the higher compositions (x > 0.70) suffer from comparatively smaller grain sizes. Additionally, the densification is also slowly reduced to 95% to 93% at x = 0.975 composition even though the sintering temperature is same. The increasing PT content and a subsequent reduction in the grain size, increases the coercive nature of the materials. The large tetragonality for high PT compositions results into very high value of the unit cell polarization. For the compositions with high PT concentration (x = 0.95 and 0.975) possess high tetragonality. Therefore, a comparatively high field is required for them for domain switching and to exhibit a well saturated P-E loop. Nonetheless, the breakdown strength of these compositions were low due to the defect losses and lower densification, which hindered the high field application in them. Thus, these

compositions show very small polarization magnitudes and higher coercivity in the measured P-E loops.

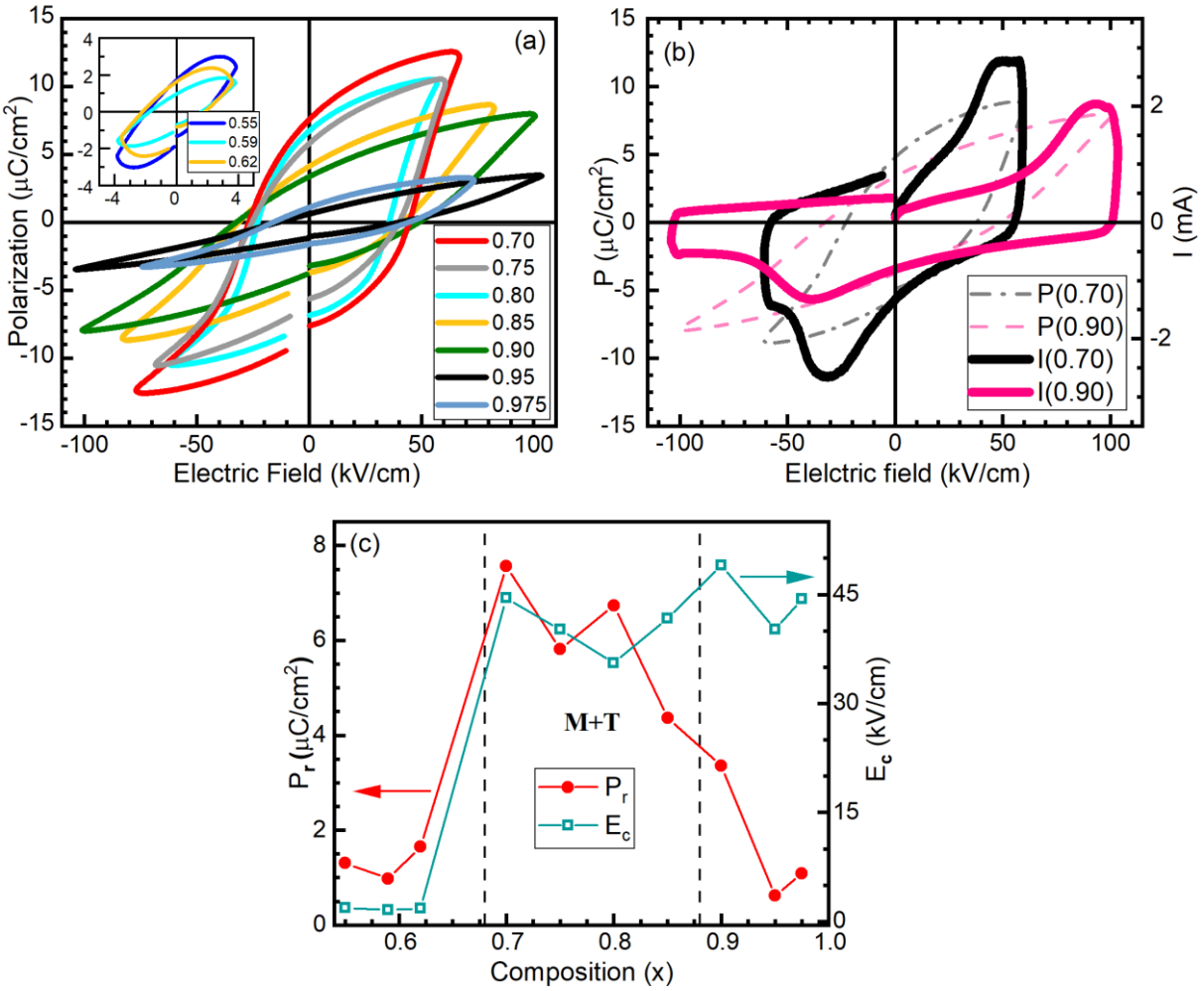

Fig 5.6 Ferroelectric characterization of (1-x)BCN-(x)PT;(a) P-E hysteresis loops for various compositions; (b) transient current-electric field loop of x = 0.70 (@65kV/cm) and x = 0.90 (@105kV/cm) compositions; (c) variation of remnant polarization and coercive field with composition

5.6 Composition Dependence of Piezoelectric Response in (1-x)BCN-(x)PT Ceramics

The piezoelectric coefficient (d_{33}) values measured on poled pellets for the composition range $0.55 \leq x \leq 0.95$ are shown in Fig 5.7(a). Higher piezoelectric responses have been observed for 0.70, 0.75 and 0.90 compositions. The piezoelectric response in this system is affected by several factors, and their correlation with the composition-dependent variation of piezoelectric response has been depicted in Fig 5.7(b). Various important factors affecting the piezoelectric response are described as follows:

(1) Leakage current in the samples that can be proportional to the concentration of Cu-ion, the higher the Cu-ion concentration the larger the probability of Cu(+1) defects. In addition to defect related to Cu-ion, the Pb and O vacancies during sintering and porosity in the sample also contributes to the leakage current. With high leakage current the d_{33} value decreases.

(2) The composition regions where MPBs are expected may exhibit larger responses of piezoelectricity, especially where monoclinic phase coexists with the other ferroelectric phases as it leads to increased number of polarization directions for the switching of the polarization vector under electric field [140].

(3) Low-temperature processing and PbO deficiency can reduce the grain size of the sintered pellets [141]. Grain size distribution can also potentially affect piezoelectricity, and larger grain sizes may show increased piezo responses.

High tetragonality of BCN and PT increases the intrinsic unit cell polarization. High unit cell level ferroelectric distortion or tetragonality is essentially desired for piezo-response in ferroelectric ceramics. However, beyond a certain value, the large unit

cell polarization can make it difficult to switch the ferroelectric domains under external field, as they will need extremely high electric field. Thus, they can restrict the observation of large piezoelectric response in such compositions as they cannot be poled efficiently.

A combined effect of all these factors contributes to the net response of the piezoelectric d_{33} coefficient, which is shown in Fig 5.7(a) for various compositions of (1-x)BCN-(x)PT ceramics. Except for the exception at x = 0.70, 0.75 and 0.90 compositions, the d_{33} shows a gradual increasing trend in the solid solution as PT concentration increases. This trend can potentially be due to the increased Pb and decreased Cu-ion concentrations. The former ion (Pb) increases dipolar polarization by additional hybridization of its $6s^2$ lone pair electrons with 2p-orbital electrons of the oxygen ions, while the latter one (Cu) can cause leakage current by the valency fluctuation and high losses originating from the defect concentration.

The compositions in region $0.05 \leq x \leq 0.55$ do not show piezoelectricity due to their full or partial crystallization in a cubic crystal structure. The composition range $0.59 \leq x \leq 0.65$ show weak piezo-response due to difficulty in proper poling because of larger leakage current. The larger increment of d_{33} for x = 0.70, 0.75 and 0.90 compositions of the solid solution is linked with the appearance of crystallographic phase boundaries and crystal structure changes around these compositions. Very high increment in the piezoresponse of x = 0.70 composition is observed in comparison to the 0.65 composition, while the 0.75 composition shows comparable values. Compared to x = 0.65, both the compositions (0.70 and 0.75) are calcined at high temperatures, leading to their increased grain sizes (see Fig 5.2). Both x = 0.70 and 0.75 share an

almost similar crystal structure (containing smaller monoclinic phase fractions). Only slight difference in grain sizes and density is found in these compositions. This further supports the phase-coexistence proximity being the main responsible factor for such a high increase in the response. It can also be anticipated that the d_{33} of these compositions can be further increased if the densification is improved and leakage current is reduced for them. However, for the sake of a comparative study, the sintering temperatures for all these compositions were kept the same. For x = 0.80 and 0.85 compositions, the d_{33} decreases drastically along with a decrease in density and as well as grain sizes. Its decreased proximity to the crystal structural transition and difficulty in poling due to larger unit cell level polarization can be anticipated to be the main reason for this considerable decrement. Again, for the x = 0.90 composition, the coexisting monoclinic phase changes to a tetragonal one, while the density and grain sizes continue to exhibit decrement. This further supports the enhancement of the piezoelectric properties near this phase boundary. Table 5.1 list the values of piezoelectric strain coefficient (d_{33}) for various compositions. Maximum response is obtained for the x = 0.70 composition.

Conclusively, it can be expected that the (1-x)BCN-(x)PT solid solution may show high responses of piezoelectricity if the grain size is increased and conductivity losses of defect species are controlled. But while doing so, some other factors, such as partial melting and reduction in oxidation state of the constituent elements, etc., needs to be carefully considered and suitably addressed, while maintaining the capacity and rate of interconversion of coexisting phases, as processing variables and composition plays a vital role in the phase stabilities [77].

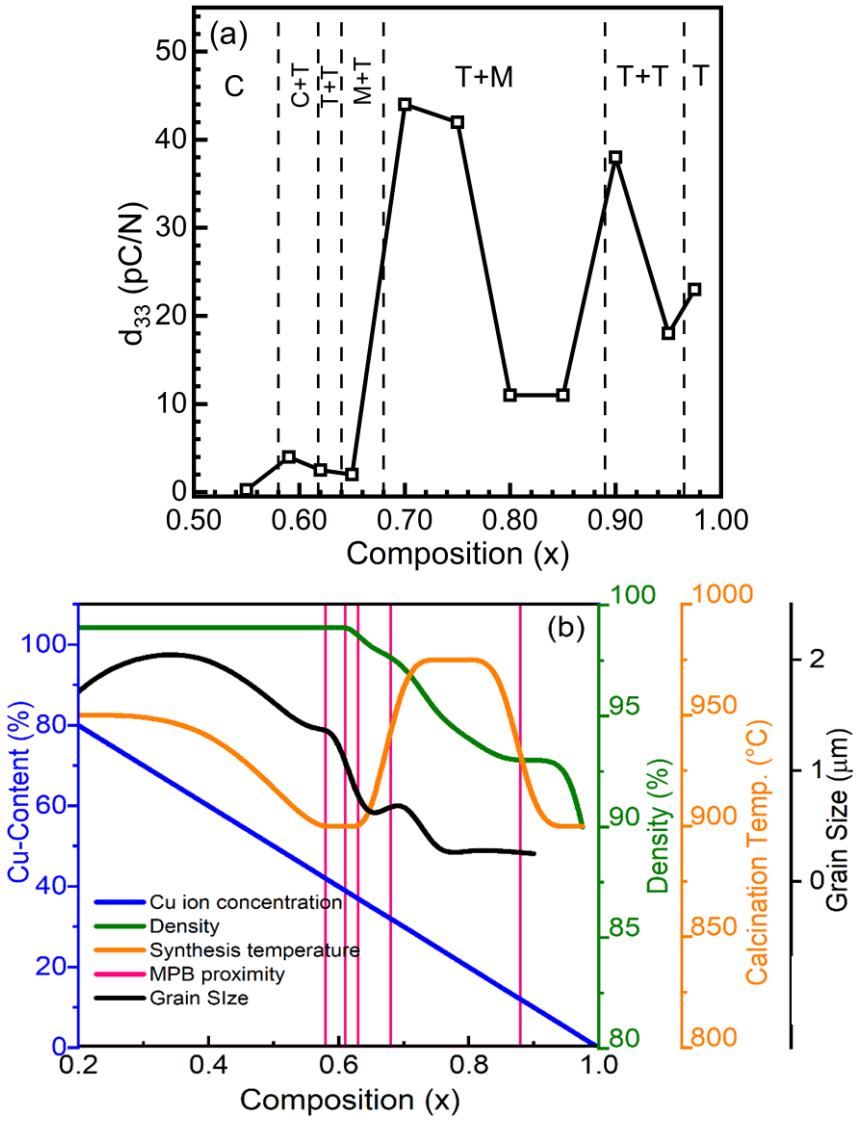

Fig 5.7 (a) Variation of piezoelectric strain coefficient (d_{33}) for (1-x)BCN-(x)PT ceramics and (b) correlation of various important factors affecting piezoelectricity.

5.7 Summary and Conclusion

This chapter presents the microstructure, dielectric, ferroelectric and piezoelectric property investigations on (1-x)BCN-(x)PT solid solution in full composition range and their correlation with the crystal structure. All the compositions are chemically homogeneous and possess desired ratio and valences of constituent ions. Interestingly,

two transition peaks are seen in the temperature-dependence of relative dielectric permittivity responses for the compositions belonging to a predominantly phase separation coexistence region $0.70 \leq x \leq 0.90$. Enhanced ferroelectricity and piezoelectricity is obtained for the composition with $x = 0.70$, having larger grain size and proximity to phase boundaries. The piezoelectric responses of the solid solution can be further improved with long-term annealing and defect engineering, which is the subject matter of the next chapter.